

## Research Article

# Role of Oxygen Vacancies in the Electrical Properties of $\text{WO}_{3-x}$ Nano/Microrods with Identical Morphology

Zhenguang Shen <sup>1,2,3</sup>, Zengying Zhao,<sup>2</sup> Jian Wen,<sup>3</sup> Jingwen Qian,<sup>1,2,3</sup>  
Zhijian Peng <sup>1,2</sup>, and Xiuli Fu <sup>3</sup>

<sup>1</sup>School of Engineering and Technology, China University of Geosciences, Beijing 100083, China

<sup>2</sup>School of Science, China University of Geosciences, Beijing 100083, China

<sup>3</sup>School of Science, Beijing University of Posts and Telecommunications, Beijing 100876, China

Correspondence should be addressed to Zhijian Peng; pengzhijian@cugb.edu.cn and Xiuli Fu; xiulifu@bupt.edu.cn

Received 9 January 2018; Revised 14 March 2018; Accepted 31 March 2018; Published 13 May 2018

Academic Editor: Mengkun Tian

Copyright © 2018 Zhenguang Shen et al. This is an open access article distributed under the Creative Commons Attribution License, which permits unrestricted use, distribution, and reproduction in any medium, provided the original work is properly cited.

Tungsten oxide ( $\text{WO}_{3-x}$ ) crystalline nano/microrods with identical morphology but different contents of oxygen vacancies were prepared by thermally evaporating fixed amount of  $\text{WO}_3$  powder in reductive atmosphere from different amounts of S power at  $1150^\circ\text{C}$  in a vacuum tube furnace, in which both sources were loaded in separate ceramic boat. With increasing amount of S powder, a series of tungsten oxides,  $\text{WO}_3$ ,  $\text{WO}_{2.90}$ ,  $\text{W}_{19}\text{O}_{55}$  ( $\text{WO}_{2.89}$ ), and  $\text{W}_{18}\text{O}_{49}$  ( $\text{WO}_{2.72}$ ), could be obtained. And devices were fabricated by screen-printing the obtained  $\text{WO}_{3-x}$  crystals on ceramic substrates with Ag-Pd interdigital electrodes. With increasing content of oxygen vacancies, the devices fabricated with  $\text{WO}_{3-x}$  crystals present a negative to positive resistance response to relative humidity. Under dry atmosphere, for the devices with increasing  $x$ , the strong response to light changed from short to long wavelength; under light irradiation, the conducting ability of the devices was enhanced, due to the more efficient separation and transportation of the photogenerated carriers; and under simulated solar irradiation, the photocurrent intensity of the  $\text{W}_{18}\text{O}_{49}$  device was roughly 8 times, about 500 times, and even 1000 times larger than that of the  $\text{W}_{19}\text{O}_{55}$ ,  $\text{WO}_{2.90}$ , and  $\text{WO}_3$  one, respectively. With the versatile optoelectrochemical properties, the obtained  $\text{WO}_{3-x}$  crystals have the great potential to prepare various humidity sensors and optoelectrical devices.

## 1. Introduction

As an important strategic nonferrous metal, the highly efficient utilization and high value-added processing of tungsten resources are of great significance. Among the various forms of tungsten materials, tungsten oxides are important semiconductors, which can be used in solar-driven photocatalysis [1–3], electrochromism [4], and photochromism [5]. In addition, tungsten oxides are highly sensitive to many kinds of gas, which are considered as one of the most promising gas sensing materials for the detection of  $\text{NH}_3$ ,  $\text{H}_2\text{S}$ ,  $\text{NO}_x$ ,  $\text{O}_3$ ,  $\text{H}_2$ , and so on [6–9].

However, due to the multiple chemical valences and complicated structure of tungsten oxides, their morphology and composition are difficult to control independently. In literatures [10, 11], it was reported that  $\text{WO}_{3-x}$  crystals with

a variety of oxygen-deficient stoichiometries like  $\text{WO}_{2.72}$ ,  $\text{WO}_{2.8}$ , and  $\text{WO}_{2.83}$  are stable under the normal condition, but their morphology might be diversified. Thus, the role of oxygen vacancy alone in the electrical properties of tungsten oxides has still been controversial [12, 13]. Moreover, because tungsten oxides are versatile materials, it would be applied in diversified conditions, such as in dry or humid atmosphere, under light irradiation, or in the dark. Therefore, it is of much significance to investigate the electrical properties of tungsten oxides with varied contents of oxygen vacancies without influencing by the morphology under different environmental conditions.

Here we propose a simple, fast, environmentally friendly, and energetically efficient thermal evaporation method for the preparation of tungsten oxides ( $\text{WO}_{3-x}$ ) crystalline nano/microrods (NMRs) in large scale with only  $\text{WO}_3$  and S

powders as the starting materials. By elaborately controlling the processing parameters, a series of tungsten oxides ( $\text{WO}_3$ ,  $\text{WO}_{2.90}$ ,  $\text{W}_{19}\text{O}_{55}$ , and  $\text{W}_{18}\text{O}_{49}$ ) of identical morphology but with different contents of oxygen vacancies were obtained. And devices were fabricated simply by screen-printing the obtained  $\text{WO}_{3-x}$  crystals onto ceramic substrates with Ag-Pd interdigital electrodes. The electrical properties of the devices are systematically investigated under different conditions. The measured results reveal that the obtained  $\text{WO}_{3-x}$  crystals have the great potential to prepare various humidity sensors and optoelectrical devices.

## 2. Experimental Section

**2.1. Materials Preparation.** The applied  $\text{WO}_3$  (Sinopharm Group Co. Ltd.) and elemental S (Aladdin Industrial Corporation) were commercially bought raw powders of analytical grade and directly used without further purification. The proposed  $\text{WO}_{3-x}$  crystalline NMRs were synthesized in an experimental vacuum, horizontal alumina tube furnace (SJG-16, China) by using a high-temperature thermal evaporation process [11].

In a typical process, an alumina boat with 1 g  $\text{WO}_3$  powder was placed at the heating center of the furnace, while another one with different amounts of S powder (0.1–0.5 g) was located on the upstream of carrier gas flow at 10 cm away from the  $\text{WO}_3$  powder. Before heating, the alumina tube was pumped out and flushed with high-purity carrier gas (here  $\text{N}_2$ , 99.99 vol.%) repeatedly for several times. Then, the furnace was heated up to 1150 °C in 1.5 h from room temperature, dwelling at this temperature for 1 h. After heating, the furnace was cooled down naturally to room temperature simply by shutting down the electricity of the heating system of the furnace. During the whole heating process, the  $\text{N}_2$  gas flow inside the alumina tube was maintained at 200 sccm. Finally, products with a color from light-green to purple-red could be obtained in the alumina boat originally loaded with  $\text{WO}_3$  raw powder.

**2.2. Materials Characterization.** X-ray diffraction (XRD, Bruker D8 diffractometer, Germany) analysis was conducted in continuous mode with  $\text{Cu K}\alpha$  radiation ( $\lambda = 1.5418 \text{ \AA}$ ). The XRD scanning range was from 10 to 60° and the speed was 6°/min. X-ray photoelectron spectroscopy (XPS, Thermo escalab 250Xi, ThermoFisher Scientific, America; non-monochromated  $\text{Mg K}\alpha$  radiation, photon energy 1253.6 eV) was used to investigate the chemical state of the elements in the samples, and the spectrometer was calibrated by the binding energy of C1s line (285 eV). Field emission scanning electron microscopy (FE-SEM, Hitachi SU8020, Japan) was used to examine the morphology of the obtained samples. The specific surface area of the obtained samples was measured by the Brunauer–Emmett–Teller (BET)  $\text{N}_2$  adsorption method using a Micromeritics ASAP2020 surface analyzer (China National Pharmaceutical Group Corp., Shanghai, China). Electron spinning resonance (ESR, JEOL JES-FA200, Japan) was carried out at room temperature with a microwave frequency of 9.44 GHz to investigate the unpaired electron and defect in the samples. And diphenylpicrylhydrazyl was used

for the  $g$  value calibration. The electrochemical impedance spectroscopy (EIS) was performed on an electrochemical workstation (CHI 660D, Chenghua Instrument Company, China) in a frequency from 100 kHz to 0.1 Hz with an open circuit potential at an AC perturbation of 0.1 V.

**2.3. Fabrication and Measurement of Devices.** 0.1 g of each product was first ground and then mixed with 1 mL of absolute ethanol to form a paste. After that, 0.1 mL of the prepared pastes was spinning-coated by a coater (KW-4 A, China) at a rotational speed of 1000 rpm for 20 s onto an alumina ceramic substrate (Company Elitetech, China) with a size of 6 mm in length, 3 mm in width, and 0.5 mm in thickness, where the screen had already been printed with two Ag-Pd interdigital electrodes of five fingers with a distance of 0.15 mm. Finally, a device was fabricated by drying it at room temperature for 1 h.

The characteristic  $I$ - $V$  curves in different levels of relative humidity were measured with an operating voltage from 0 to +3 V and an operating frequency of 1000 Hz. The controlled relative humidity was obtained by using saturated salt solution method as reported in [14, 15]. The applied six different saturated salt solutions in this work were prepared by LiCl,  $\text{MgCl}_2$ ,  $\text{Mg}(\text{NO}_3)_2$ , NaCl, KCl, and  $\text{KNO}_3$ , which could provide a relative humidity at 25 °C of approximately 11%, 33%, 54%, 75%, 85%, and 95%, respectively. Before measurement, each device was first soaked at 25 °C in an atmosphere of different levels of relative humidity in the six chambers with different salt solutions till it reached the adsorption-desorption equilibrium for water.

The characteristic  $I$ - $V$  curves of the devices were also recorded in dry atmosphere under the irradiation with light of different wavelengths (400 and 600 nm) and simulated solar irradiation (SSI), respectively. The SSI was provided by a 300 W xenon lamp (PLS-SXE300, Beijing Perfect Light Co. Ltd., China), and the light of different wavelengths was realized by adding different optical filters. During the tests, the  $I$ - $V$  curves of the devices were first measured in the dark, and then the measurements were carried out under different lights after 5 min of irradiation. In addition, the photocurrent measurement was performed at a voltage of 1 V under SSI.

## 3. Results and Discussion

**3.1. Composition, Structure, and Morphology of  $\text{WO}_{3-x}$  Nanomaterials.** Figure 1(a) shows the XRD patterns of typical products fabricated by thermal evaporation of 1 g  $\text{WO}_3$  powder and different amounts of S powders at 1150 °C. When the applied amount of S was 0.1 g, the obtained sample was still of pure monoclinic  $\text{WO}_3$  phase (JCPDS no. 43-1035). When it increased to 0.15 g, a pure monoclinic phase of  $\text{WO}_{2.90}$  would be acquired. Its XRD peaks can perfectly match with those in the standard JCPDS card no. 36-0102. When 0.2 g of S was applied, the resultant sample was composed of a pure monoclinic phase of  $\text{W}_{19}\text{O}_{55}$  (JCPDS no. 45-0167). However, when the applied amount of S was between 0.25 and 0.3 g, a mixture of  $\text{W}_4\text{O}_{11}$  and  $\text{W}_5\text{O}_{14}$  would be produced (please see Figure S1 in Supplementary Materials). As the applied amount of S increased to 0.5 g, a pure monoclinic phase of

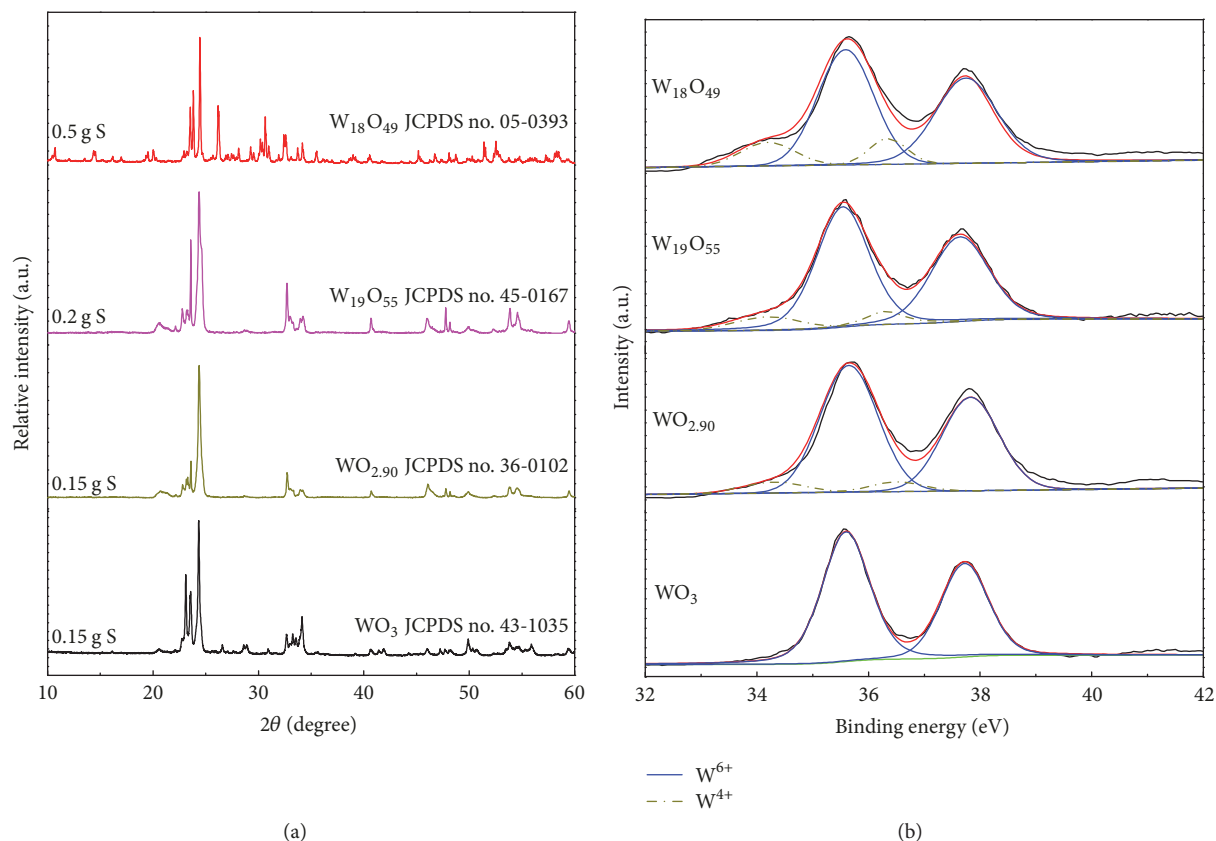


FIGURE 1: XRD (a) and XPS (b) patterns of the obtained samples. The samples were prepared by thermal evaporation of 1 g  $\text{WO}_3$  powder and different amounts of S powders (0.1–0.5 g) at  $1150^\circ\text{C}$  separately. The results indicate that pure  $\text{WO}_3$ ,  $\text{WO}_{2.90}$ ,  $\text{W}_{19}\text{O}_{55}$ , and  $\text{W}_{18}\text{O}_{49}$  crystals could be obtained, when the applied amount of S was 0.1, 0.15, 0.2, and 0.5 g of S, respectively.

$\text{W}_{18}\text{O}_{49}$  (JCPDS no. 05-0393) was attained. According to our previous studies [11], if the applied amount of S was further increased (e.g., up to 1 g),  $\text{WS}_2$  phase would appear in the samples, because at such high temperature the excessive S vapor would take all the O atoms away from some of the tungsten oxides, finally resulting in  $\text{WS}_2$  phase. Therefore, in the present work, in order to obtain pure  $\text{WO}_{3-x}$  crystals with different contents of oxygen vacancies, the applied amount of S was selected between 0.1 and 0.5 g.

The surface chemical state of the obtained samples was examined by XPS analysis with the high-resolution spectra of W4f (please also check Figure S2). The obtained W4f patterns and the fitted results after a Shirley background subtraction are shown in Figure 1(b). From this figure, it was revealed that the W4f core-level spectrum could be fitted into two doublets, in association with two different oxidation states of W atoms. The peak couples (solid blue curve) at 35.55 and 37.64 eV (with a binding energy gap of 2.09 eV and peak area ratio of about 4:3) correspond to  $\text{W}^{6+}$ , respectively. Meanwhile, the peak couples (dash-dot dark yellow) have binding energies of  $\text{W}^{4+}_{7/2} = 33.75$  eV and  $\text{W}^{4+}_{5/2} = 35.22$  eV (with a binding energy gap of 2.1 eV and peak area ratio of roughly 4:3), which agree well with  $\text{W}^{4+}$  state [16]. From this figure, it can be seen that the  $\text{WO}_{2.90}$ ,

$\text{WO}_{2.89}$ , and  $\text{WO}_{2.72}$  samples all contain the two oxidation states of tungsten ( $\text{W}^{4+}$  and  $\text{W}^{6+}$ ), but with increasing  $x$ , the proportion of  $\text{W}^{4+}$  increases and the mean valence of their W ions decreases from 5.61 to 5.36 (see Table S1). In addition, the  $\text{WO}_3$  sample was completely oxidized, containing only  $\text{W}^{6+}$  atoms. And all these results are well consistent with those observed from XRD analysis.

The ESR spectra of the obtained samples are displayed in Figure 2. From this figure, it could be seen that the ESR spectra of the oxygen-deficient  $\text{WO}_{3-x}$  crystals exhibit a sharp signal at  $g = 2.28$ , while that of  $\text{WO}_3$  presents no obvious signals. The signal of the present oxygen-deficient  $\text{WO}_{3-x}$  compounds could be attributed to oxygen vacancies, because it presents a similar  $g$  value with those of the already reported metal oxides, in which the peak assigned to oxygen vacancies always has a  $g$  factor of about 2.01 [10, 17, 18]. Furthermore, in metal oxides, most of the excessive electrons are localized at the oxygen vacancies sites, and, usually, one oxygen vacancy bounds one extra electron; and the sharp  $g$  signal of metal oxides would become stronger with increasing concentration of oxygen vacancies [17, 19]. Here in this work, the shift of the  $g$  value for the present oxygen-deficient  $\text{WO}_{3-x}$  compounds to a higher value might be owing to the presence of two charge centers (two unpaired electrons) trapped in the oxygen

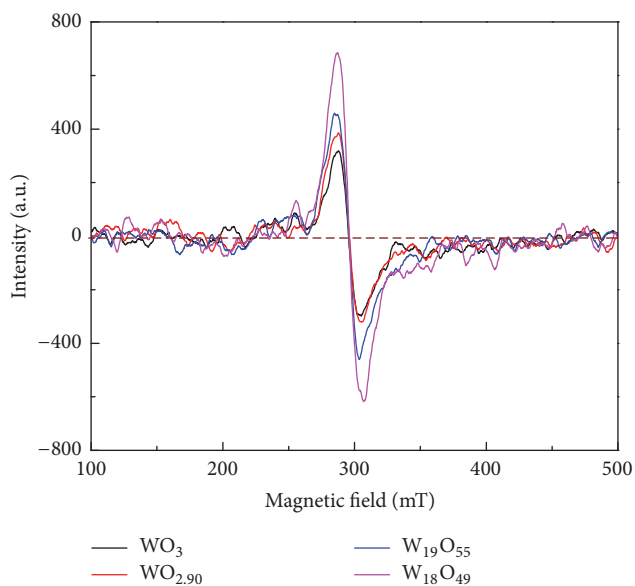


FIGURE 2: ESR spectra of the obtained  $\text{WO}_{3-x}$  samples.

vacancy [10, 18]; and, with increasing  $x$ , the sharp  $g$  signal gets stronger and stronger, indicating that there are more oxygen vacancies in the obtained  $\text{WO}_{3-x}$  samples. But there is no signal in the ESR spectrum of  $\text{WO}_3$ , implying that the sample of  $\text{WO}_3$  was completely oxidized. And this result is well consistent with those from XPS analysis.

The morphology of the obtained samples prepared by thermal evaporation of 1 g  $\text{WO}_3$  powder and 0.1–0.5 g of S powders at  $1150^\circ\text{C}$  was examined by SEM. Typical SEM images of the above-mentioned samples are displayed in Figure 3. For more information, please check Figure S3. SEM examination revealed that, under the present conditions, all the obtained samples had identical morphology, presenting a microstructure of many NMRs. The BET surface areas of the samples were almost the same (please check Figure S4). With a rough evaluation, the diameter of the NMRs was in the range of 100 nm to  $5\ \mu\text{m}$ , and the length of them was about 30 to  $50\ \mu\text{m}$ . According to our previous study [11], the growth of the present tungsten oxide nanorods was controlled by a vapor-solid mechanism.

**3.2. Electrical Properties.** EIS is a powerful tool to study electrochemical behavior of a semiconductor, especially the phenomena of charge transfer [20–22]. The EIS data are displayed in Figure 4. The inset shows an equivalent circuit for the devices.  $R_s$  is the external resistance,  $Q_1$  is the constant phase element (CPE), and  $R_{t1}$  is the charge transfer resistance across the interface. It is seen that the Nyquist plots of the as-synthesized  $\text{WO}_3$  and  $\text{WO}_{2.90}$  both present a complete semicircle, while those of  $\text{W}_{19}\text{O}_{55}$  and  $\text{W}_{18}\text{O}_{49}$  only show a trend for a semicircle, possibly because, with increasing  $x$ , the semiconductivity of  $\text{WO}_{3-x}$  decreased and the metallicity increased. But with the increase of oxygen vacancies, the arc radius of the EIS Nyquist plots presents a sharp decrease, indicating a decrease in the solid state

interface layer resistance and the charge transfer resistance on the surface [3]. This result also suggests that, with the increase of oxygen vacancies, the charge carriers transfer efficiency of  $\text{WO}_{3-x}$  increased.

To evaluate the kinetics of charge transfer of the devices fabricated with the obtained  $\text{WO}_{3-x}$  crystals under different levels of relative humidity, the complex impedance characteristics of the humidity devices were investigated. The EIS spectra are shown in Figures 5(a)–5(d). The EIS data of the devices fabricated with  $\text{WO}_3$  are presented in Figure 5(a). As can be seen from this figure, at low relative humidity (11–33%), a semicircle was observed in the complex plot, indicating a “non-Debye” behavior in the materials, due to a kind of polarization [14]. Moreover, the impedance is extremely high, because the dominant electron conduction is difficult due to the least content of oxygen vacancies in the present  $\text{WO}_3$  among all the  $\text{WO}_{3-x}$  crystals. In addition, although the ionic conduction (here also called electrolytic conduction) existed mainly due to the hopping of  $\text{H}^+$  on the material surface [15], the conducting film was discontinuous at low humidity. With the increase of relative humidity (54–95%), plots with a semicircle at high frequency followed with a straight line at low frequency were recorded. That phenomenon was caused by the  $\text{H}_3\text{O}^+$  and  $\text{H}^+$  traveling via the exchange of the Grotthuss chain mechanism [15]. The line represents Warburg impedance, owing to the diffusion of the electroactive species at the electrodes [14]. Figure 5(b) shows the EIS data of the devices fabricated with  $\text{WO}_{2.90}$ . Similarly with  $\text{WO}_3$  devices, it can be clearly seen that a semicircle was observed in the complex impedance plots at low relative humidity (11–33%). But at high relative humidity (54–95%), it is quite clear that the straight line appeared at low frequency would present at a higher relative humidity than that of  $\text{WO}_3$ , due to the fact that the content of oxygen vacancy in  $\text{WO}_{2.90}$  is much higher than that in  $\text{WO}_3$ . Moreover, because there are even more oxygen vacancies in  $\text{W}_{19}\text{O}_{55}$  and  $\text{W}_{18}\text{O}_{49}$ , they exhibit unique impedance plots as shown in Figures 5(c) and 5(d). At low humidity, only a small amount of water molecules would be adsorbed. Because the coverage of the water molecules adsorbed on the device surface is not continuous, the electrolytic conduction is difficult. The conduction mode is mainly electron conduction due to the vast oxygen vacancies in  $\text{W}_{19}\text{O}_{55}$  and  $\text{W}_{18}\text{O}_{49}$ . With increasing relative humidity, a large amount of water molecules would be absorbed by oxygen vacancies, which will result in a continuous electrolytic film. Then the electron conduction becomes less dominant, while the contribution of electrolytic conduction will increase. However, due to the largest amount of oxygen vacancies, the device prepared with  $\text{W}_{18}\text{O}_{49}$  may be still dominated by electron conduction at a fairly higher relative humidity. The equivalent circuits of the devices are shown in Figure 5(e).  $R_s$  is the external resistance,  $Q_1$  and  $Q_2$  are the constant phase elements (CPE),  $R_{t1}$  is the charge transfer resistance across the interface, and  $R_{t2}$  is the impedance at the electrode/device film interface. For the devices,  $R_{t1} \ll R_{t2}$  at low RH, and the impedance change of the devices is mostly determined by  $R_{t1}$ . At high RH, the magnitudes of  $R_{t1}$  and  $R_{t2}$  are the same and the impedance change of the devices is determined by both  $R_{t1}$  and  $R_{t2}$ .

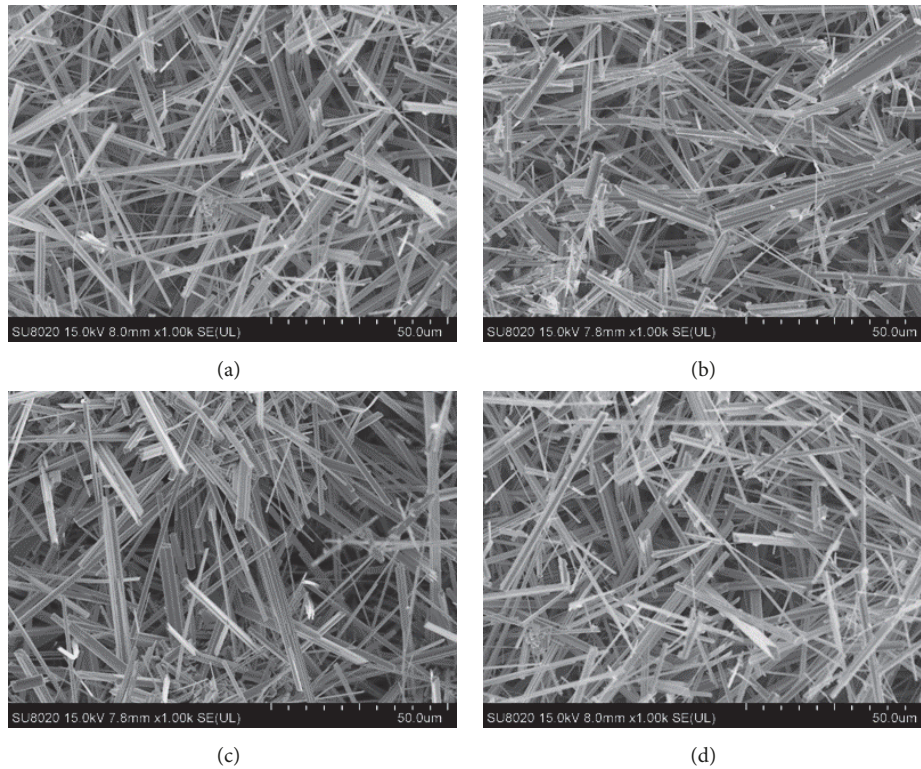


FIGURE 3: Typical SEM images of the samples prepared by thermal evaporation of 1g  $\text{WO}_3$  powder and different amounts of S powders at  $1150^\circ\text{C}$  separately: (a) 0.1, (b) 0.15, (c) 0.2, and (d) 0.5 g.

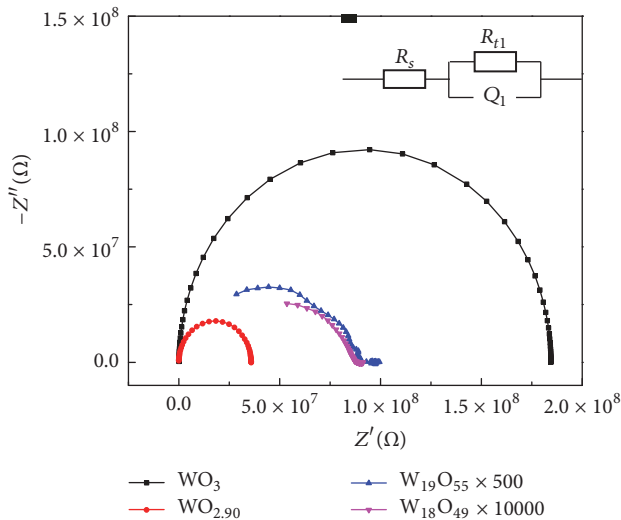


FIGURE 4: Electrochemical impedance spectra of the devices fabricated with the obtained  $\text{WO}_{3-x}$  crystals with different contents of oxygen vacancies. The inset shows an equivalent circuit for the devices.

The characteristic  $I$ - $V$  curves of the devices fabricated with the obtained  $\text{WO}_{3-x}$  crystals were first measured at different levels of relative humidity, and the results are shown in Figure 6. From Figure 6(a), it can be seen that, for the device fabricated with  $\text{WO}_3$ , with the increase of relative

humidity, the slope of the curve increased gradually. For the  $\text{WO}_{2.90}$  and  $\text{W}_{19}\text{O}_{55}$  devices (see Figures 6(b) and 6(c)), however, with increasing humidity, the slope of the curves first decreased at low relative humidity (11–54%) and then increased at high relative humidity (75%–95%). Specifically, for the  $\text{WO}_{2.90}$  device, the slope of the curve under a relative humidity of 75% is greater than that under a relative humidity of 11% (see Figure 6(b)), and for the  $\text{W}_{19}\text{O}_{55}$  device, the slopes of the curve under a relative humidity of 95% are smaller than that under a relative humidity of 54% (see Figure 6(c)). And with the increase of the relative humidity, the slope of the curve of the  $\text{W}_{18}\text{O}_{49}$  device decreased gradually (see Figure 6(d)). Because the reciprocal of the slope of  $I$ - $V$  curve represents the measured resistance, so from Figure 6, it can be deduced that, with the increase of relative humidity, the resistance of the device fabricated with  $\text{WO}_3$  decreases gradually; those of the  $\text{WO}_{2.90}$  and  $\text{W}_{19}\text{O}_{55}$  devices increase first and then decrease; and that of the  $\text{W}_{18}\text{O}_{49}$  device increases gradually. The response and recovery characteristic of the sensors fabricated with the obtained tungsten oxide crystals is shown in Figure S5. In a word, with more oxygen vacancies, the devices fabricated with  $\text{WO}_{3-x}$  crystals present a negative to positive resistance response to relative humidity, showing the great potential for preparing varied humidity sensors.

A possible qualitative mechanism to explain the humidity sensing properties of the obtained tungsten oxide crystals can be proposed hereafter. For the device fabricated with  $\text{WO}_3$ , because there is no oxygen vacancy in  $\text{WO}_3$  crystal,

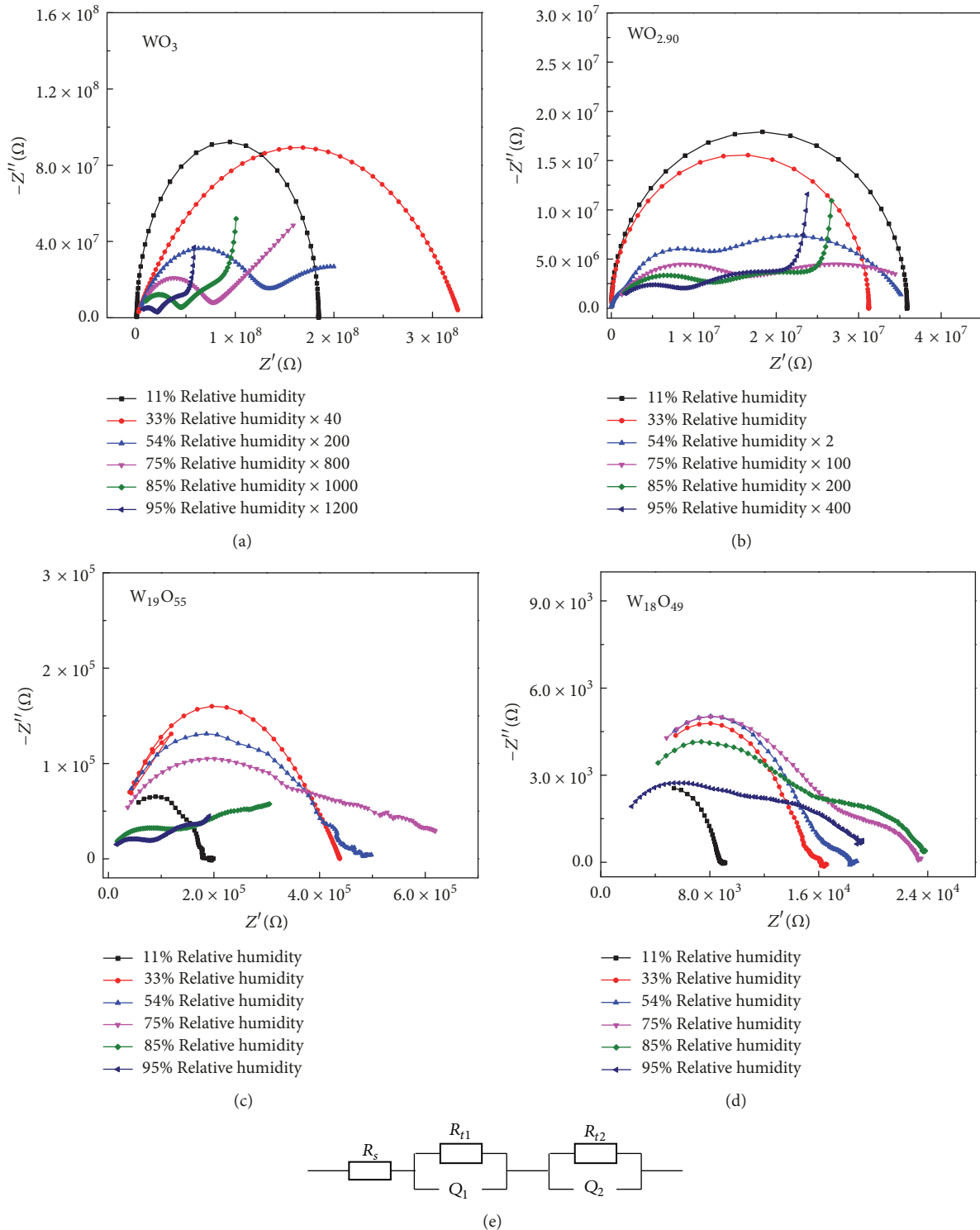


FIGURE 5: Electrochemical impedance spectra of the devices fabricated with the obtained  $\text{WO}_{3-x}$  crystals in different levels of relative humidity: (a)  $\text{WO}_3$ , (b)  $\text{WO}_{2.90}$ , (c)  $\text{W}_{19}\text{O}_{55}$ , and (d)  $\text{W}_{18}\text{O}_{49}$ ; and the equivalent circuits of the devices (e).

with the increase of humidity more water molecules would be adsorbed to the surface of the  $\text{WO}_3$  crystal. As a result, the electrical conductivity would increase, because the water-related electrolytic conduction mainly functionalizes as a

surface mechanism [23]. In literature, it was reported that, oxygen vacancies would bound electrons as free carriers [24, 25], and thus they could introduce donor levels between the conduction and valence bands [10, 26], which would

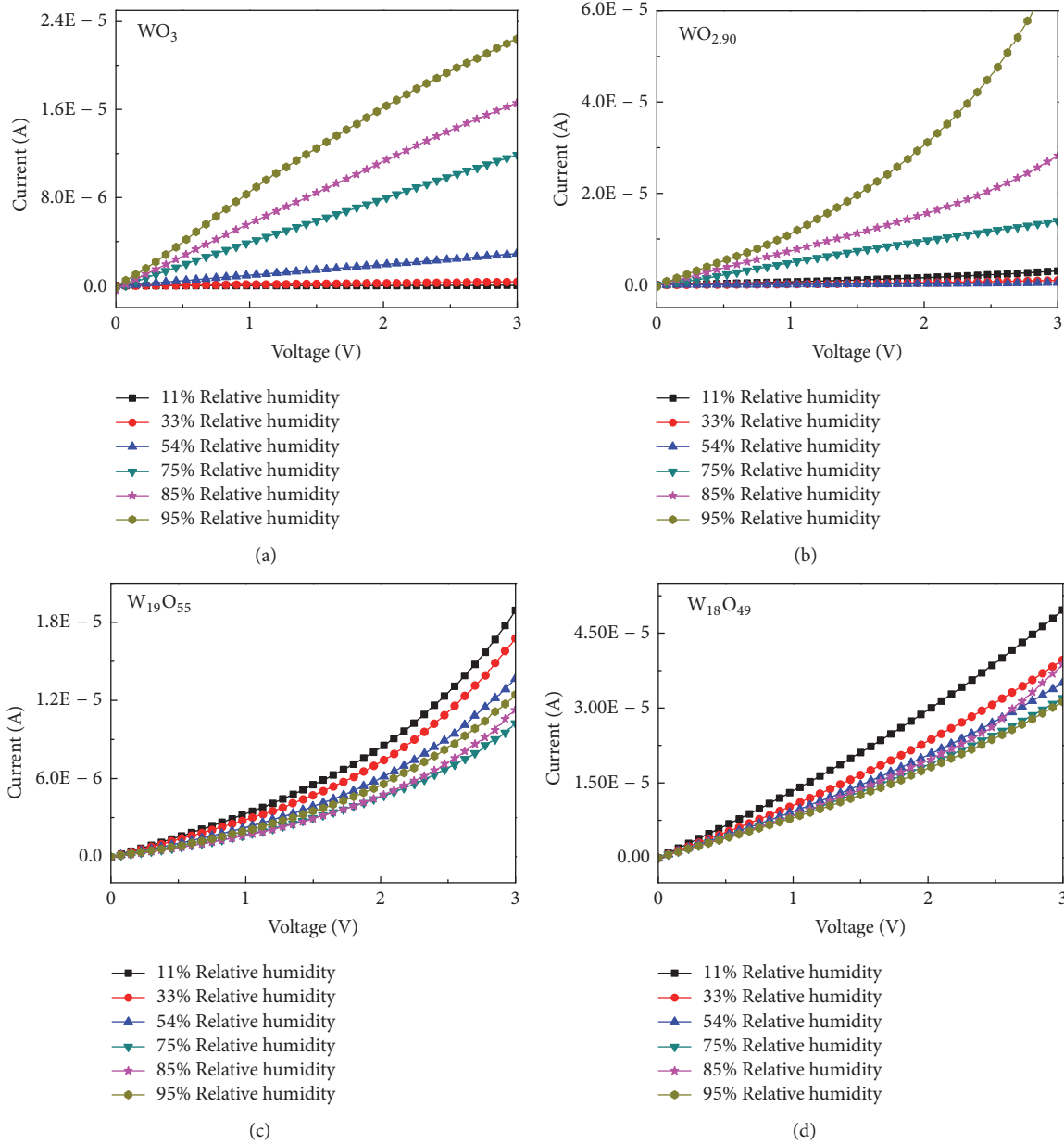


FIGURE 6: Characteristic  $I-V$  curves of the devices fabricated with the obtained  $WO_{3-x}$  crystals in different levels of relative humidity: (a)  $WO_3$ , (b)  $WO_{2.90}$ , (c)  $W_{19}O_{55}$ , and (d)  $W_{18}O_{49}$ .

result in increased conductivity for semiconducting oxides. For the  $WO_{2.90}$  and  $W_{19}O_{55}$  devices, the oxygen vacancies induced conduction mechanism would compete with the water-related surface mechanism, which might even become dominating in the transport process at low humidity. With increasing relative humidity, water molecules would be absorbed by oxygen vacancies, which will result in a continuous electrolytic film on the crystal surface. Then the electron conduction becomes less dominant, while the contribution of electrolytic conduction will increase, causing the resistance of the  $WO_{2.90}$  and  $W_{19}O_{55}$  devices to increase first and then decrease. But compared with  $WO_{2.90}$  device,

because there are more oxygen vacancies in  $W_{19}O_{55}$  device, the electrolytic conduction would be dominated in higher relative humidity. However, due to the largest amount of oxygen vacancies, the device prepared with  $W_{18}O_{49}$  may still be dominated by electron conduction at a fairly higher relative humidity. So, with the relative humidity increased from 11% to 95%, the resistance of  $W_{18}O_{49}$  device continued to increase.

To examine the electrical properties of the devices fabricated with the obtained  $WO_{3-x}$  crystals in diversified environments, the characteristic  $I-V$  curves were also measured in the dark and under SSI. Generally, the characteristic  $I-V$

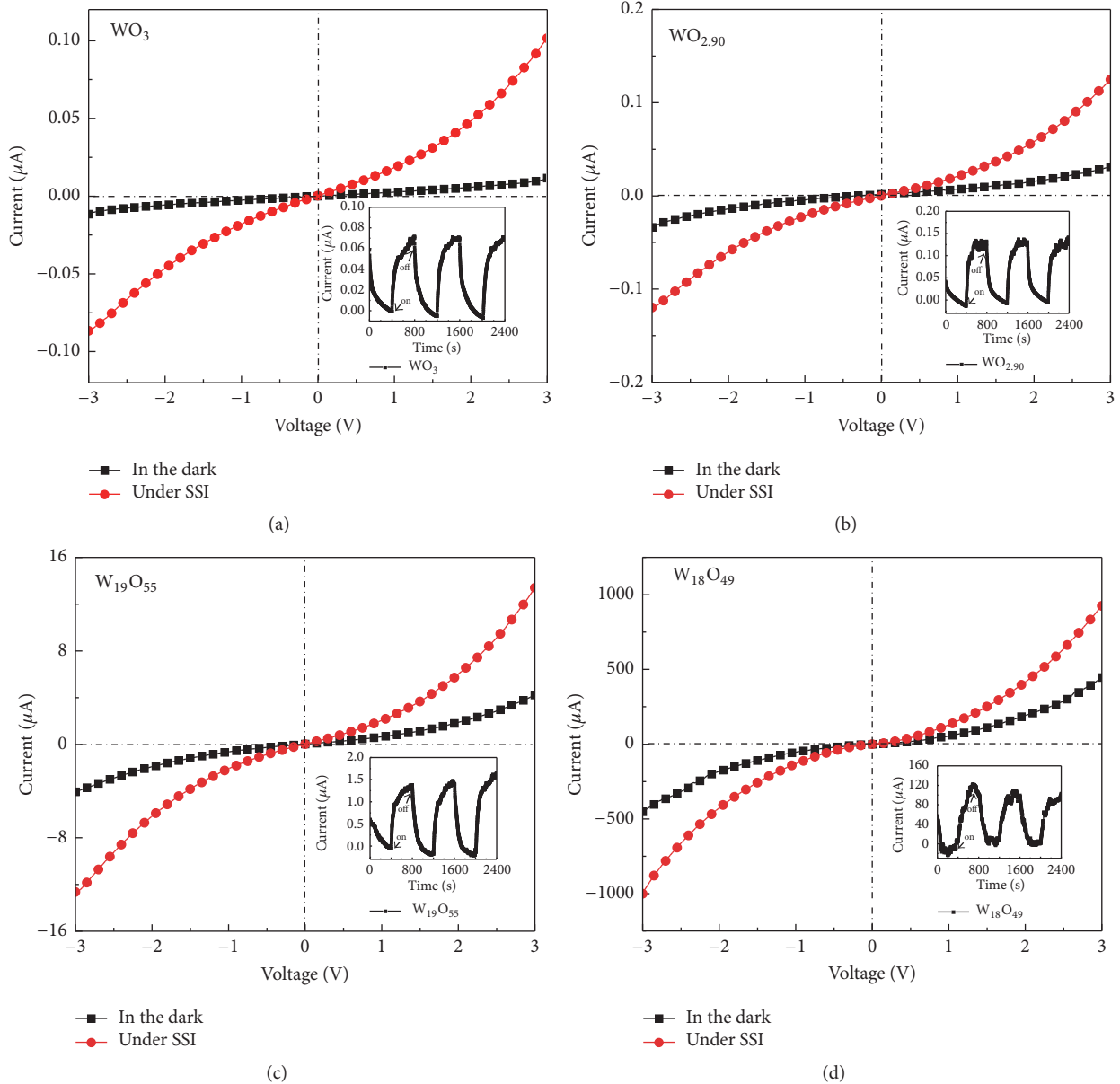


FIGURE 7: Characteristic  $I$ - $V$  curves of the devices fabricated with the obtained  $\text{WO}_{3-x}$  crystals under different light atmospheres, in which the insets display their photocurrent responses: (a)  $\text{WO}_3$ , (b)  $\text{WO}_{2.90}$ , (c)  $\text{W}_{19}\text{O}_{55}$ , and (d)  $\text{W}_{18}\text{O}_{49}$ .

curves of one-dimensional nanomaterials are linear [27, 28], rectifying [29–32], asymmetric [29, 33], or symmetric [27, 34, 35]. For the present devices, normally, the contact of metal electrodes with the  $\text{WO}_{3-x}$  crystals would be either a Schottky barrier or an Ohmic contact. As is seen from Figure 7, all the  $I$ - $V$  curves of the devices fabricated with the obtained  $\text{WO}_{3-x}$  crystals are symmetric, indicating the existence of Schottky barriers between the metal electrodes and  $\text{WO}_{3-x}$  crystals. Therefore, the  $\text{WO}_{3-x}$  crystals synthesized in this work are semiconducting. With the increase of  $x$ , the content of oxygen vacancies increases and thus the conductivity becomes stronger, because oxygen vacancies act as shallow donors for metal oxides [36]. Moreover, in literature, it was reported that the lifetime and yield of the photogenerated electrons and the

holes in  $\text{WO}_3$  and similar materials would increase, which can be proven by transient absorption spectroscopy [37, 38]. In this work, under SSI, it was found that the conductivity of all the devices was improved and, with the increase in  $x$ , the added value of the conductivity increased. In our previous work [11], it was revealed that the band-gap of the  $\text{WO}_{3-x}$  crystals decreased with the increase of  $x$ . As a result, the absorption range of the spectrum would be expanded, leading to an enhanced absorption efficiency of light by the  $\text{WO}_{3-x}$  crystals, and thus more photoelectrons would be produced during illumination, resulting in the higher photocurrents and increased conductivity. In addition, through analyzing the resultant photocurrent-time ( $I$ - $t$ ) profiles displayed in the insets of Figure 7, it was revealed that, under SSI, the

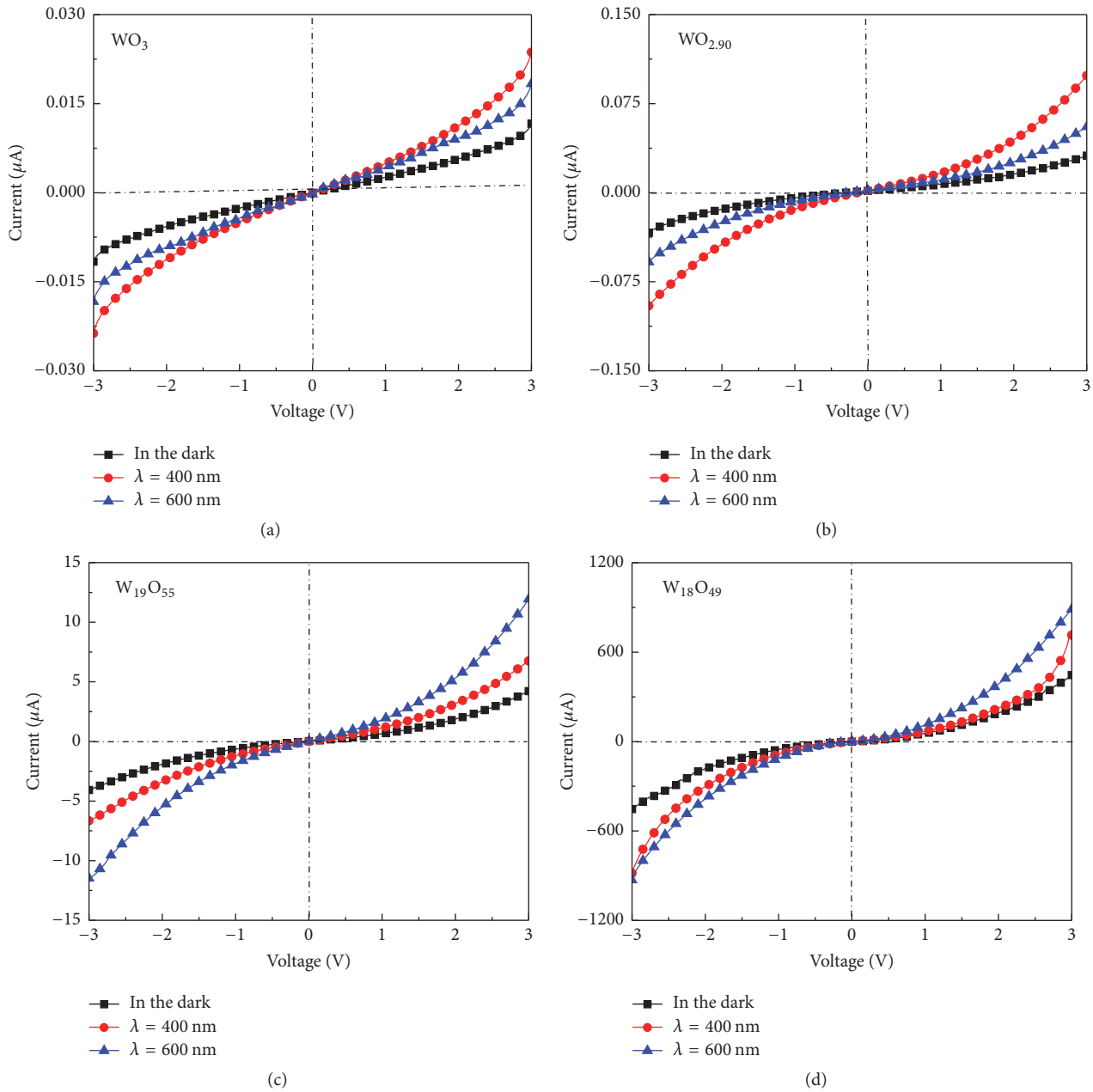


FIGURE 8: Characteristic  $I$ - $V$  curves of the devices fabricated with the obtained  $\text{WO}_{3-x}$  crystals under irradiation of light with different wavelengths (400 and 600 nm): (a)  $\text{WO}_3$ , (b)  $\text{WO}_{2.90}$ , (c)  $\text{W}_{19}\text{O}_{55}$ , and (d)  $\text{W}_{18}\text{O}_{49}$ .

produced photocurrents are reproducible and stable during three light-on/off cycles. Under SSI, the electrons and holes separated and gradually increased to form photocurrents. But when the light was shut off, electrons would no longer be produced and might recombine with the original holes. Thus, the photocurrents will gradually decrease. Comparatively, the photocurrent intensity of the  $\text{W}_{18}\text{O}_{49}$  device was roughly 8 times, about 500 times, and even 1000 times larger than that of the  $\text{W}_{19}\text{O}_{55}$ ,  $\text{WO}_{2.90}$ , and  $\text{WO}_3$  one, respectively. For the  $\text{WO}_{3-x}$  crystals with more oxygen vacancies, the dramatic increase in photocurrent response for the light-on/off could mainly be ascribed to the enhanced absorption efficiency of

light by the  $\text{WO}_{3-x}$  crystals under illumination and possibly their faster separation and transportation of photogenerated  $e^-$  on the surface of the working electrodes [36, 39]. This result is consistent with that of the UV-vis measurement in our previous work [11].

Due to the different contents of oxygen vacancies in the present  $\text{WO}_{3-x}$  crystals, their band-gaps are different, which will respond to different wavelengths of light. Thus, the characteristic  $I$ - $V$  curves of the devices fabricated with the obtained  $\text{WO}_{3-x}$  crystals under the irradiation of light with different wavelengths (400 and 600 nm) were investigated. The results are illustrated in Figure 8. For comparison, those

measured in the dark are also presented. As can be seen from this figure, all the characteristic  $I$ - $V$  curves measured in the dark and under the light irradiation are symmetric, indicating the existence of Schottky barriers between the metal electrodes and  $\text{WO}_{3-x}$  crystals. Under the irradiation of light with different wavelengths (400 and 600 nm), it was found that the conductivity of the devices was enhanced, mainly due to the improved separation of electrons and holes in the  $\text{WO}_{3-x}$  crystals generated under illumination. Moreover, it can be seen from Figures 8(a) and 8(b) that, for the  $\text{WO}_3$  and  $\text{WO}_{2.90}$  devices, with a shorter wavelength of light, under irradiation, the conductivity became stronger. However, for the  $\text{W}_{19}\text{O}_{55}$  and  $\text{W}_{18}\text{O}_{49}$  devices, with a longer wavelength of light, under irradiation, the conductivity got better (see Figures 8(c) and 8(d)). These phenomena can be attributed to the fact that  $\text{WO}_3$  and  $\text{WO}_{2.90}$  have larger band-gap than  $\text{W}_{19}\text{O}_{55}$  and  $\text{W}_{18}\text{O}_{49}$ . In summary, with increasing  $x$ , the devices present their strong response to the light of short to long wavelength, showing that the as-synthesized  $\text{WO}_{3-x}$  crystals have great potential for preparing various optoelectrical devices.

#### 4. Conclusions

By changing the ratio of  $\text{WO}_3$  to S, a series of  $\text{WO}_{3-x}$  crystalline NMRs of identical morphology but with different contents of oxygen vacancies were successfully prepared through thermally evaporating  $\text{WO}_3$  in reductive S atmosphere from different amounts of S powder loaded separately in a vacuum furnace. With the obtained  $\text{WO}_{3-x}$  crystals, devices were fabricated simply by screen-printing the obtained  $\text{WO}_{3-x}$  crystals onto ceramic substrates with Ag-Pd interdigital electrodes. With increasing content of oxygen vacancies, the prepared devices present a negative to positive resistance response to relative humidity. Under dry atmosphere, with increasing  $x$ , the devices present their strong response to the light of short to long wavelength. With more oxygen vacancies, under light irradiation, the conducting ability of the devices was enhanced, due to the more efficient separation and transportation of the photogenerated carriers. Under simulated solar irradiation, the photocurrent intensity of the  $\text{W}_{18}\text{O}_{49}$  device was roughly 8 times, about 500 times, and even 1000 times larger than that of the  $\text{W}_{19}\text{O}_{55}$ ,  $\text{WO}_{2.90}$ , and  $\text{WO}_3$  one, respectively. All these results reveal that the obtained  $\text{WO}_{3-x}$  crystals have the great potential for preparing various humidity sensors and optoelectrical devices.

#### Conflicts of Interest

The authors declare that they have no conflicts of interest.

#### Acknowledgments

The authors would like to thank the financial support for this work from the National Natural Science Foundation of China (Grants nos. 11674035 and 61274015) and Excellent Adviser Foundation in China University of Geosciences from the Fundamental Research Funds for the Central Universities.

#### Supplementary Materials

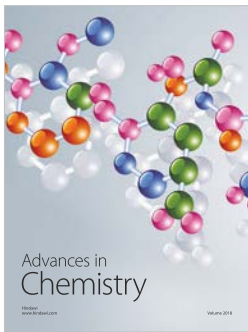
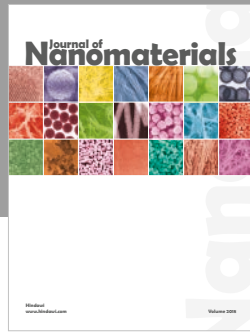
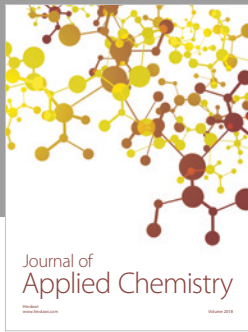
The composition, structure, and morphology of  $\text{WO}_{3-x}$  nanomaterials. The response-recovery characteristic curves and response-recovery times of the sensors fabricated with the obtained  $\text{WO}_{3-x}$  crystals. Figure S1: XRD patterns of the samples synthesized by thermal evaporation of 1 g  $\text{WO}_3$  powder with different amounts of S powder at 1150°C. These results reveal that the obtained samples consist of tungsten oxides ( $\text{WO}_{3-x}$ ) with different contents of oxygen vacancies. Figure S2: full spectra of the samples synthesized by thermal evaporation of 1 g  $\text{WO}_3$  powder with different amounts of S powder at 1150°C: (a) 0.1, (b) 0.15, (c) 0.2, (d) 0.25, (e) 0.3, and (f) 0.5 g. It can be seen that all the samples elementally consist of W and O (please also check Table S1). Figure S3: typical SEM images of the samples synthesized by thermal evaporation of 1 g  $\text{WO}_3$  powder with different amounts of S powder at 1150°C: (a) 0.1, (b) 0.15, (c) 0.2, (d) 0.25, (e) 0.3, and (f) 0.5 g. It can be seen that all the samples almost have identical morphology. Figure S4:  $\text{N}_2$  adsorption-desorption isotherms of the obtained  $\text{WO}_{3-x}$  samples. The isotherms are characteristic of a type IV isotherm with a type H3 hysteresis loop, indicating that they are mesoporous structures in the samples. The BET surface areas of the  $\text{WO}_3$ ,  $\text{WO}_{2.90}$ ,  $\text{W}_{19}\text{O}_{55}$ , and  $\text{W}_{18}\text{O}_{49}$  samples were determined approximately as 1.18, 1.06, 1.03, and 0.95  $\text{m}^2/\text{g}$ , while the volume of the adsorbed  $\text{N}_2$  by them under the relative pressure of 1.0 was 1.41, 2.13, 2.40, and 4.70  $\text{cm}^3/\text{g}$ , respectively. Figure S5: response-recovery characteristic curves (a) and response-recovery times (b) of the sensors fabricated with the obtained  $\text{WO}_{3-x}$  crystals. Table S1 Table 1: the content of W ions in the obtained tungsten oxides samples determined by XPS and their average/theoretical average oxidation number of W. (*Supplementary Materials*)

#### References

- [1] N. Zhang, C. Chen, Z. Mei et al., "Monoclinic tungsten oxide with 100 facet orientation and tuned electronic band structure for enhanced photocatalytic oxidations," *ACS Applied Materials & Interfaces*, vol. 8, no. 16, pp. 10367–10374, 2016.
- [2] M. Seifollahi Bazarjani, M. Hojamberdiev, K. Morita et al., "Visible light photocatalysis with c- $\text{WO}_{3-x}/\text{WO}_3 \times \text{H}_2\text{O}$  nanoheterostructures in situ formed in mesoporous polycarbosilane-siloxane polymer," *Journal of the American Chemical Society*, vol. 135, no. 11, pp. 4467–4475, 2013.
- [3] J. Qian, Z. Zhao, Z. Shen, G. Zhang, Z. Peng, and X. Fu, "Oxide vacancies enhanced visible active photocatalytic  $\text{W}_{19}\text{O}_{55}$  NMRs via strong adsorption," *RSC Advances*, vol. 6, no. 10, pp. 8061–8069, 2016.
- [4] L. Xiao, Y. Lv, W. Dong, N. Zhang, and X. Liu, "Dual-functional  $\text{WO}_3$  nanocolumns with broadband antireflective and high-performance flexible electrochromic properties," *ACS Applied Materials & Interfaces*, vol. 8, no. 40, pp. 27107–27114, 2016.
- [5] A. I. Gavrilyuk, "Aging of the nanosized photochromic  $\text{WO}_3$  films and the role of adsorbed water in the photochromism," *Applied Surface Science*, vol. 364, pp. 498–504, 2016.
- [6] Y.-A. Lee, S. S. Kalanur, G. Shim, J. Park, and H. Seo, "Highly sensitive gasochromic  $\text{H}_2$  sensing by nano-columnar  $\text{WO}_3$ -Pd

- films with surface moisture," *Sensors and Actuators B: Chemical*, vol. 238, pp. 111–119, 2017.
- [7] Y. L. Wang, J. Liu, X. B. Cui et al., "NH<sub>3</sub> gas sensing performance enhanced by Pt-loaded on mesoporous WO<sub>3</sub>," *Sensors and Actuators B: Chemical*, vol. 238, pp. 473–481, 2017.
- [8] Z. Wang, M. Hu, Y. Wang, X. Liu, and Y. Qin, "Effect of solvothermal reaction temperature on the morphology of WO<sub>3</sub> nanocrystals and their low-temperature NO<sub>2</sub>-sensing properties," *Journal of Alloys and Compounds*, vol. 665, pp. 173–179, 2016.
- [9] Y. R. Wang, B. Liu, S. H. Xiao et al., "Low-temperature H<sub>2</sub>S detection with hierarchical Cr-doped WO<sub>3</sub> microspheres," *ACS Applied Materials & Interfaces*, vol. 8, no. 15, pp. 9674–9683, 2016.
- [10] J. Qian, Z. Peng, Z. Shen, Z. Zhao, G. Zhang, and X. Fu, "Positive impedance humidity sensors via single-component materials," *Scientific Reports*, vol. 6, Article ID 25574, 2016.
- [11] Z. Shen, Z. Zhao, J. Qian, Z. Peng, and X. Fu, "Synthesis of WO<sub>3-x</sub> nanomaterials with controlled morphology and composition for highly efficient photocatalysis," *Journal of Materials Research*, vol. 31, no. 8, pp. 1065–1076, 2016.
- [12] A. N. Gunnar, B. Lars, and L. Anna-Lena, "Electrochromic tungsten oxide: the role of defects," *Solar Energy Materials & Solar Cells*, vol. 84, no. 1–4, pp. 315–328, 2004.
- [13] M. Gillet, C. Lemire, E. Gillet, and K. Aguir, "The role of surface oxygen vacancies upon WO<sub>3</sub> conductivity," *Surface Science*, vol. 532–535, pp. 519–525, 2003.
- [14] Q. Qi, T. Zhang, Q. Yu et al., "Properties of humidity sensing ZnO nanorods-base sensor fabricated by screen-printing," *Sensors and Actuators B: Chemical*, vol. 133, no. 2, pp. 638–643, 2008.
- [15] R. Wang, X. Liu, Y. He et al., "The humidity-sensitive property of MgO-SBA-15 composites in one-pot synthesis," *Sensors and Actuators B: Chemical*, vol. 145, no. 1, pp. 386–393, 2010.
- [16] M. Li, M. Hu, D. Jia, S. Ma, and W. Yan, "NO<sub>2</sub>-sensing properties based on the nanocomposite of n-WO<sub>3-x</sub>/n-porous silicon at room temperature," *Sensors and Actuators B: Chemical*, vol. 186, pp. 140–147, 2013.
- [17] Y. Nosaka, M. Nishikawa, and A. Y. Nosaka, "Spectroscopic investigation of the mechanism of photocatalysis," *Molecules*, vol. 19, no. 11, pp. 18248–18267, 2014.
- [18] C. Di Valentin and G. Pacchioni, "Spectroscopic properties of doped and defective semiconducting oxides from hybrid density functional calculations," *Accounts of Chemical Research*, vol. 47, no. 11, pp. 3233–3241, 2014.
- [19] R. Klaysri, S. Wichaidit, T. Tubchareon et al., "Impact of calcination atmospheres on the physicochemical and photocatalytic properties of nanocrystalline TiO<sub>2</sub> and Si-doped TiO<sub>2</sub>," *Ceramics International*, vol. 41, no. 9, pp. 11409–11417, 2015.
- [20] S. J. Hong, S. Lee, J. S. Jang, and J. S. Lee, "Heterojunction BiVO<sub>4</sub>/WO<sub>3</sub> electrodes for enhanced photoactivity of water oxidation," *Energy & Environmental Science*, vol. 4, no. 5, pp. 1781–1787, 2011.
- [21] S. Banerjee, S. K. Mohapatra, P. P. Das, and M. Misra, "Synthesis of coupled semiconductor by filling ID TiO<sub>2</sub> nanotubes with CdS," *Chemistry of Materials*, vol. 20, no. 21, pp. 6784–6791, 2008.
- [22] A. T. Mane, S. T. Navale, and V. B. Patil, "Room temperature NO<sub>2</sub> gas sensing properties of DBSA doped PPy-WO<sub>3</sub> hybrid nanocomposite sensor," *Organic Electronics*, vol. 19, pp. 15–25, 2015.
- [23] B. M. Kulwicki, "Humidity sensors," *Journal of the American Ceramic Society*, vol. 74, no. 4, pp. 697–708, 1991.
- [24] A. Janotti and C. G. Van De Walle, "Oxygen vacancies in ZnO," *Applied Physics Letters*, vol. 87, no. 12, Article ID 122102, 3 pages, 2005.
- [25] Y.-S. Liu, C.-Y. Hsieh, Y.-J. Wu et al., "Mechanism of conductivity degradation of AZO thin film in high humidity ambient," *Applied Surface Science*, vol. 282, pp. 32–37, 2013.
- [26] R. Schaub, P. Thostrup, N. Lopez et al., "Oxygen vacancies as active sites for water dissociation on rutile TiO<sub>2</sub>(110)," *Physical Review Letters*, vol. 87, no. 26, Article ID 266104, 4 pages, 2001.
- [27] F. Yi, Y. Huang, Z. Zhang, Q. Zhang, and Y. Zhang, "Photoluminescence and highly selective photoresponse of ZnO nanorod arrays," *Optical Materials*, vol. 35, no. 8, pp. 1532–1537, 2013.
- [28] Y. Cui, X. F. Duan, J. T. Hu, and C. M. Lieber, "Doping and electrical transport in silicon nanowires," *The Journal of Physical Chemistry B*, vol. 104, no. 22, pp. 5213–5216, 2000.
- [29] C. S. Lao, J. Liu, P. Gao et al., "ZnO nanobelt/nanowire schottky diodes formed by dielectrophoresis alignment across au electrodes," *Nano Letters*, vol. 6, no. 2, pp. 263–266, 2006.
- [30] S. Ranwa, P. Kumar Kulriya, V. Dixit, and M. Kumar, "Temperature dependent electrical transport studies of self-aligned ZnO nanorods/Si heterostructures deposited by sputtering," *Journal of Applied Physics*, vol. 115, no. 23, Article ID 233706, 2014.
- [31] Y. Caglar, A. Arslan, S. Ilcan, E. Hür, S. Aksoy, and M. Caglar, "Preparation and characterization of electrodeposited ZnO and ZnO:Co nanorod films for heterojunction diode applications," *Journal of Alloys and Compounds*, vol. 574, pp. 104–111, 2013.
- [32] X. Liu, C. Wang, J. Xu et al., "Fabrication of ZnO/CdS/Cu<sub>2</sub>ZnSnS<sub>4</sub> p-n heterostructure nanorod arrays via a solution-based route," *CrystEngComm*, vol. 15, no. 6, pp. 1139–1145, 2013.
- [33] J. Luo, Y. Xing, J. Zhu et al., "Structure and electrical properties of Ni nanowire/multiwalled-carbon nanotube/amorphous carbon nanotube feterojunctions," *Advanced Functional Materials*, vol. 16, no. 8, pp. 1081–1085, 2006.
- [34] M. Feng, M. Zhang, J.-M. Song, X.-G. Li, and S.-H. Yu, "Ultralong silver trimolybdate nanowires: Synthesis, phase transformation, stability, and their photocatalytic, optical, and electrical properties," *ACS Nano*, vol. 5, no. 8, pp. 6726–6735, 2011.
- [35] Y. Liu, Z. Y. Zhang, Y. F. Hu, C. H. Jin, and L. Peng, "Quantitative fitting of nonlinear current-voltage curves and parameter retrieval of semiconducting nanowire, nanotube and nanoribbon devices," *Journal of Nanoscience and Nanotechnology*, vol. 8, no. 1, pp. 252–258, 2008.
- [36] X. Wang, K. Maeda, A. Thomas et al., "A metal-free polymeric photocatalyst for hydrogen production from water under visible light," *Nature Materials*, vol. 8, no. 1, pp. 76–80, 2009.
- [37] F. M. Pesci, A. J. Cowan, B. D. Alexander, J. R. Durrant, and D. R. Klug, "Charge carrier dynamics on mesoporous WO<sub>3</sub> during water splitting," *The Journal of Physical Chemistry Letters*, vol. 2, no. 15, pp. 1900–1903, 2011.
- [38] A. Morais, C. Longo, J. R. Araujo, M. Barroso, J. R. Durrant, and A. F. Nogueira, "Nanocrystalline anatase TiO<sub>2</sub>/reduced graphene oxide composite films as photoanodes for photoelectrochemical water splitting studies: the role of reduced graphene oxide," *Physical Chemistry Chemical Physics*, vol. 18, no. 4, pp. 2608–2616, 2016.

- [39] S. Zhang, Y. Yang, Y. Guo et al., "Preparation and enhanced visible-light photocatalytic activity of graphitic carbon nitride/bismuth niobate heterojunctions," *Journal of Hazardous Materials*, vol. 261, pp. 235–245, 2013.



**Hindawi**  
Submit your manuscripts at  
[www.hindawi.com](http://www.hindawi.com)

